

# Intergalactic baryon-rich regions at high redshift

A. Gayler Harford<sup>1</sup>, Andrew J. S. Hamilton<sup>2</sup>, Nickolay Y. Gnedin<sup>3</sup>

<sup>1</sup>*JILA and National Institute of Standards & Technology, Boulder, CO 80309, USA*

<sup>2</sup>*JILA, Dept. Astrophysical & Planetary Sciences, Box 440, U. Colorado, and National Institute of Standards & Technology, Boulder CO 80309, USA;*

<sup>3</sup>*Particle Astrophysics Center, Fermilab, Batavia, IL 60510, USA;*

*Kavli Institute for Cosmological Physics, Chicago, IL 60637, USA;*

*Dept. Astronomy & Astrophysics, U. of Chicago, Chicago, IL 60637 USA*

2 December 2021

## ABSTRACT

Using a high resolution cosmological simulation of reionization we have examined the differing structures formed by gas and dark matter at a redshift of 5.1. Baryon-rich regions form a small number of filaments, which connect the largest galaxies in the simulation. More detailed examination of the ten largest galaxies reveals long, slender gaseous filaments about 5 proper kpc in width radiating from the galaxy centers. Extending out from each filament are a few smooth, thin, nearly planar gaseous sheets. By contrast, the dark matter concentrates into quasi-spherical bodies. The results have implications for our understanding of structure formation in the early universe and of the Lyman alpha forest.

**Key words:** cosmology: theory – large scale structure – filaments – sheets – pancakes – baryons

## 1 INTRODUCTION

During the first gigayear of the universe the first stars, galaxies, and black holes formed, and reionization was completed. Most of the matter resided in the intergalactic medium, forming a network of sheets and filaments (for reviews see Meiksin 2007, Barkana & Loeb 2007). In this environment galaxies grew by accreting dark matter and gas to form the “cosmic web” of walls and filaments of clusters of galaxies that characterize the visible large scale structure of the universe today.

Gravitational clustering produces sheets and filaments naturally, because gravitational collapse of ellipsoidal maxima occurs at different times along the three unequal axes (Lin et al. 1965; Zel’dovich 1970; Jing & Suto 2002; Shen et al. 2006). Collapse occurs first along a single axis to produce a two dimensional sheet. Subsequent collapse of a sheet along a second axis produces a filament. Finally, collapse of filaments leads to quasi-spherical galactic haloes. Because matter clusters at various scales and with a range of overdensities, all three kinds of structure may coexist at a single moment in time. Cosmological simulations using a variety of cosmological models confirm that sheets and filaments occur generically and ubiquitously (for discussion see Valinia et al. 1997, Bond et al. 1996, Shandarin et al. 1995, Schmalzing et al. 1999, Sheth et al. 2003, and Shen et al. 2006; for reviews of early theoretical work see Shandarin et al. 1983, Shandarin & Zel’dovich 1989).

At large scales, baryons and dark matter are expected to trace the same structures. Cosmological hydrodynamic simulations with resolutions in the tens of kiloparsecs have borne this out, although differences in the smoothness of the gas and dark matter have been noted (Cen et al. 1994; Miralda-Escudé et al. 1996; Hernquist et al. 1996; Zhang et al. 1998).

On smaller scales, hydrodynamic processes may be expected to lead to some separation of baryons and dark matter. The purpose of the present paper is to explore this separation using a cosmological simulation that has sub-kiloparsec resolution and includes a detailed and careful treatment of baryonic physics (Harford & Gnedin 2007). The simulation includes 3-dimensional radiative transfer of radiation produced self-consistently by star formation, and it follows the detailed ionization and chemistry of atomic hydrogen, molecular hydrogen, and helium. We focus on an epoch at high redshift following reionization. The Jeans length changes by more than an order of magnitude over the course of reionization (see Gnedin et al. 2003 and references therein).

The simulation method has been validated in several respects. First, galaxy luminosity functions compare favorably to observations (Harford & Gnedin 2007; Harford & Gnedin 2003). Second, the reionization history is consistent with the spectra of high redshift quasars (Gnedin & Fan 2006). Finally, considerable progress has been made in reproducing

the frequency of Lyman limit systems (Kohler & Gnedin 2007).

In examining the output of the simulation reported here, we were struck by the marked difference in the distribution of baryons and dark matter on scales small enough that hydrodynamic processes are important, but large enough that intergalactic structure is easily visible. We noticed that intergalactic gas tends to occur in long, nearly continuous filaments and attached sheets, which are unusually rich in baryons relative to the cosmic mean. These filaments form “backbones” to which large, dark matter dominated galaxies are attached. In contrast, the dark matter tends to occur in many small, quasi-spherical clumps.

This paper presents evidence for these baryon-rich structures, and characterizes them.

## 2 THE SIMULATION

The simulation used in this paper was run with a “Softened Lagrangian Hydrodynamics” (SLH-P<sup>3</sup>M) code (Gnedin 1995; Gnedin & Bertschinger 1996). The simulation has a flat  $\Lambda$ CDM cosmology, with values of cosmological parameters determined by the first year WMAP data (Spergel et al 2003):  $\Omega_m = 0.27$ ,  $\Omega_b = 0.04$ ,  $\sigma_8 = 0.91$ , and  $h = 0.71$ . The mean baryonic fraction is therefore 0.148. We focus on an epoch at redshift 5.135. The computational expense to run this simulation to significantly later times is prohibitive.

Each dimension of the simulation box is  $8h^{-1}$  Mpc comoving, and contains 256 Lagrangian simulation cells. The gas dynamics is followed on a quasi-Lagrangian mesh which is gradually deformed during the simulation to achieve better resolution in high density regions. In the post processing stage, in order to compare dark matter and baryons in a similar manner, we convert each cell of the quasi-Lagrangian mesh into a “gas particle” with the same physical properties (mass, momentum, temperature, etc.) The positions of an equal number of dark matter particles of constant mass  $2.73 \times 10^6 M_\odot$  are computed with the P<sup>3</sup>M algorithm using a softening length of 0.08 kpc proper. The best resolution is limited to about 2-3 times the softening length.

The reionization process is simulated by including star formation by the Schmidt law and radiative transfer by the optically thin variable Eddington tensor method (OTVET) (Gnedin & Abel 2001). Also included are radiative transfer effects of molecular hydrogen, whose formation and dissociation are followed. A two-level implicit scheme is used to compute the effects of a hydrogen and helium plasma.

We analyze the simulation on a grid with cell size of 40 kpc comoving ( $28.4h^{-1}$  kpc comoving), equal to 6.52 kpc proper at a redshift of 5.135. This cell size is about 80 times the softening length. This choice of grid cell size, comparable to the size of a small galaxy, is a deliberate one. The grid cell size is small enough to bring out the separation of baryons and dark matter produced by hydrodynamical processes, but large enough to map regions of overdensity as low as  $10^{1.75}$ , about 56, with good signal-to-noise. We find this overdensity to be a convenient lower limit to differentiate the filamentary structure. Results for other grid cell sizes and other redshifts are explored in an Appendix.

The spatial resolution at any point in the simulation

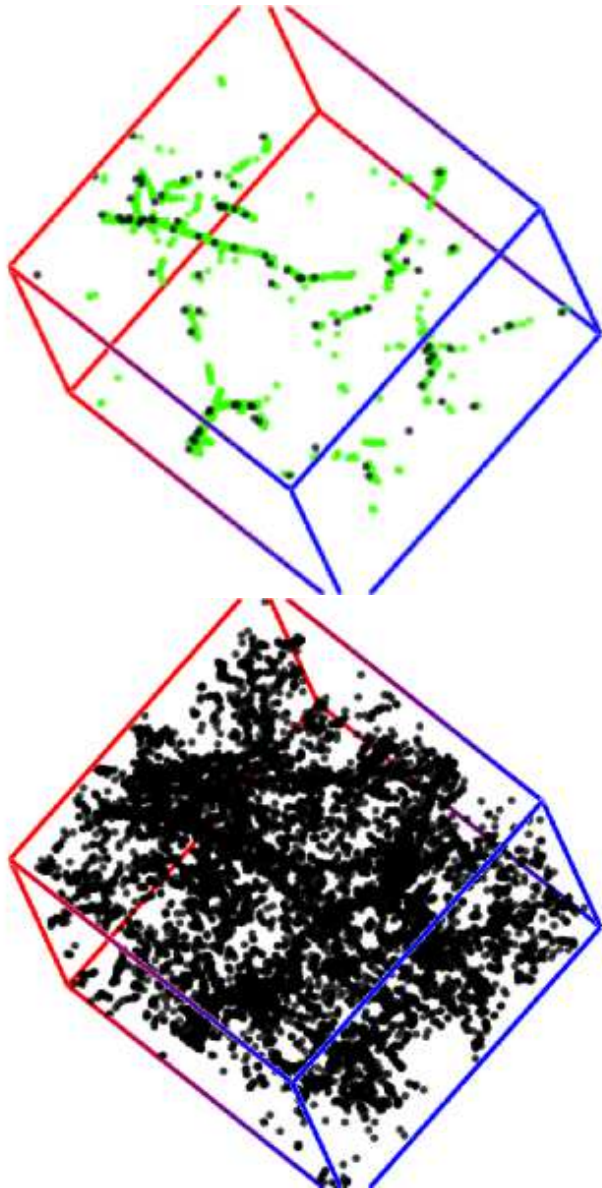


**Figure 1.** The dense regions in the simulation box at redshift 5.1. Upper: All regions of overdensity 56 or higher that are enriched in baryons to at least twice the cosmic mean are shown in translucent green. The centers of the 88 largest galaxies, those having a minimum total mass of  $10^{10} M_\odot$ , are shown as black dots. Densities and baryonic fractions were computed on grid cells 6.5 kpc proper on a side. The simulation box is 1837 proper kpc on a side at this redshift. Lower: Same as upper but showing instead all regions whose baryonic fraction are less than twice the cosmic mean.

depends upon the local density of the Lagrangian simulation cells, which is roughly proportional to the local overdensity. However, the proportionality breaks down in regions of very high or very low baryonic fraction. We have determined that all of the baryon-enriched grid cells with a minimum overdensity of 56 at  $z = 5.1$  have a minimum of 60 gas particles, each of which corresponds to a cell of the simulation. The unenriched grid cells may have fewer gas particles, and consequently lower resolution.

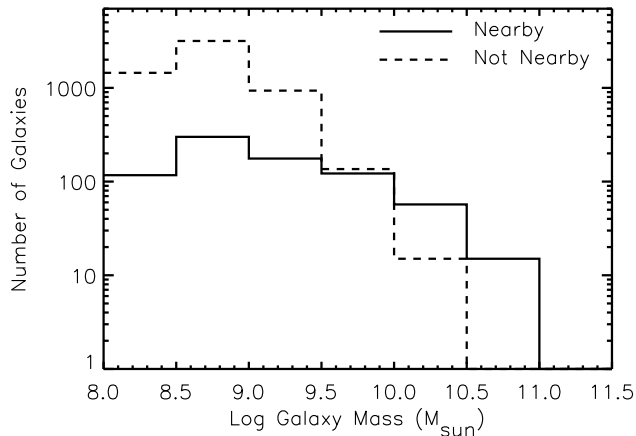


**Figure 2.** Number of galaxies with centers that are (solid line) or are not (dashed line) within two grid cells of a baryon-rich cell shown in Figure 1. Numbers are shown as a function of total galaxy mass. All galaxies above  $10^{10.5} M_{\odot}$  are nearby including one above  $10^{11} M_{\odot}$ .

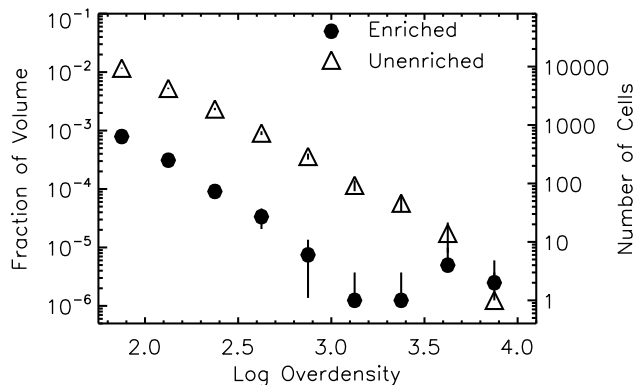


**Figure 3.** Fraction of the volume of the simulation box occupied by gas that is enriched or unenriched in baryons, as a function of overdensity in 6.5 kpc grid cells having an overdensity of 56 or higher. Threshold for baryon enrichment is twice the cosmic mean. Vertical lines show two sigma errors. Symbols are placed at the centers of the overdensity bins.

Unless otherwise noted all distances in this paper are proper.

### 3 BARYON-RICH FILAMENTS

The upper panel of Figure 1 illustrates how the baryon-rich regions in the simulation form a network of filaments. The baryon-rich regions, plotted in translucent green, are grid cells whose total overdensity is at least 56, and whose baryon fraction is at least twice the cosmic mean. Both gas and stellar matter in the simulation are included as baryons in this paper. The stellar mass in a region is usually much less than the gas mass, and generally we have not examined it separately.

The baryon-rich filaments are associated with the largest galaxies in the simulation. The upper panel of Figure 1 shows, as black spheres, the 88 largest galaxies in

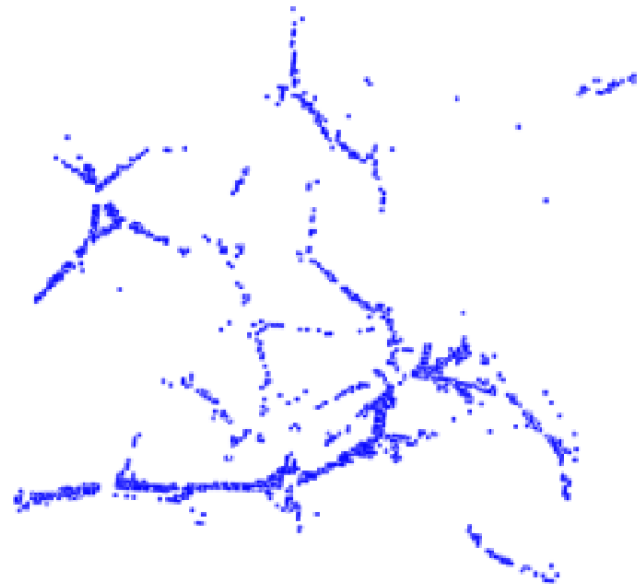
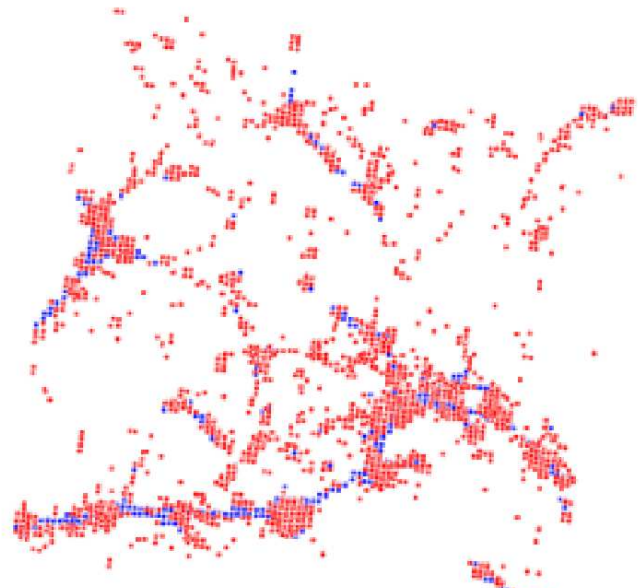


**Figure 4.** Zoom-in of the longest filament of Figure 1, again showing only 6.5 kpc grid cells with an overdensity of 56 or higher. Upper: Cells enriched in baryons to at least twice the cosmic mean are shown in dark blue; those not so enriched are in lighter red. Lower: Same, but only the dark blue enriched cells are shown for clarity. The width of the images is about 600 kpc.

the simulation, those with a total mass of at least  $10^{10} M_{\odot}$  in dark matter and baryons. Galaxies were identified with the DENMAX algorithm (Bertschinger & Gelb 1991) as gravitationally bound density peaks containing at least 100 simulation particles. The most massive galaxy in the simulation is  $1.2 \times 10^{11} M_{\odot}$ .

Figure 2 shows how many galaxies in each mass range are within two grid cells of a baryon-rich cell (we define such cells as “nearby” hereafter). Above a mass of  $10^{10} M_{\odot}$ , 83% of the galaxies are nearby, while below this range only 11% are. The nearby galaxies account for 85% of the galactic

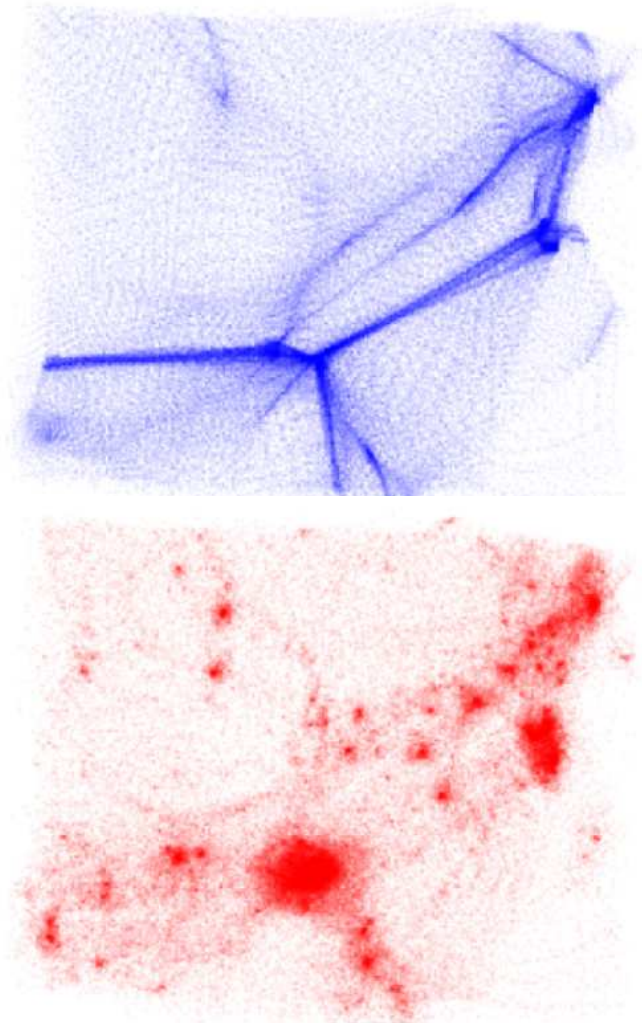


**Figure 5.** Upper: Gas simulation particles in a small region of the filament shown in Figure 4. Lower: Same view showing just dark matter particles. The width of the images is about 200 kpc.

stellar mass. Because many of the smaller galaxies are devoid of stars, only 38% of the galactic dark matter is nearby.

Although the largest galaxies in the simulation are near the baryon-rich filaments, the galaxies themselves generally have baryonic fractions close to the cosmic mean.

The baryon-rich regions are relatively rare compared to unenriched regions. The lower panel of Figure 1 shows unenriched cells with an overdensity of 56 or greater. The unenriched cells outnumber the enriched cells by a factor of about 20. The unenriched regions, though clustered, are not as strikingly filamentary as the enriched regions.

Figure 3 shows that baryon-rich cells constitute about 1/20th of the volume of unenriched cells, almost independent of overdensity. The Figure shows only overdensities 56 or above because the determination of baryon fraction becomes increasingly uncertain at lower overdensities. The Figure suggests a slight trend for greater enrichment at lower overdensity, but the statistical significance is not large.

Figure 4 shows a zoom-in of the longest enriched filament in Figure 1. The zoom-in shows large galaxies as clumps of unenriched grid cells arranged along a baryon-

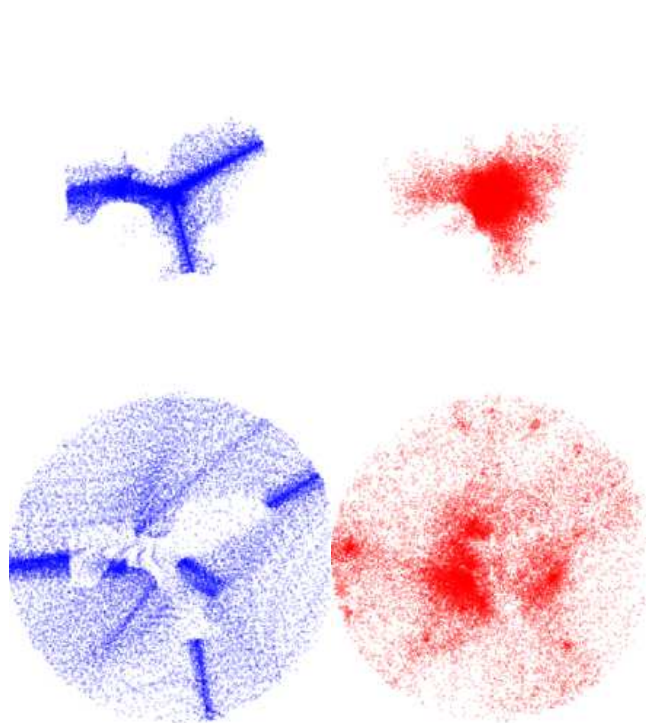


**Figure 6.** Bound and unbound gas (blue) and dark matter (red) particles within a radius of 55.4 kpc (proper) of the second largest galaxy at redshift of 5.1. Upper left: gas bound to galaxy, upper right: dark matter bound to galaxy, lower left: gas not bound to galaxy, lower right: dark matter not bound to galaxy.

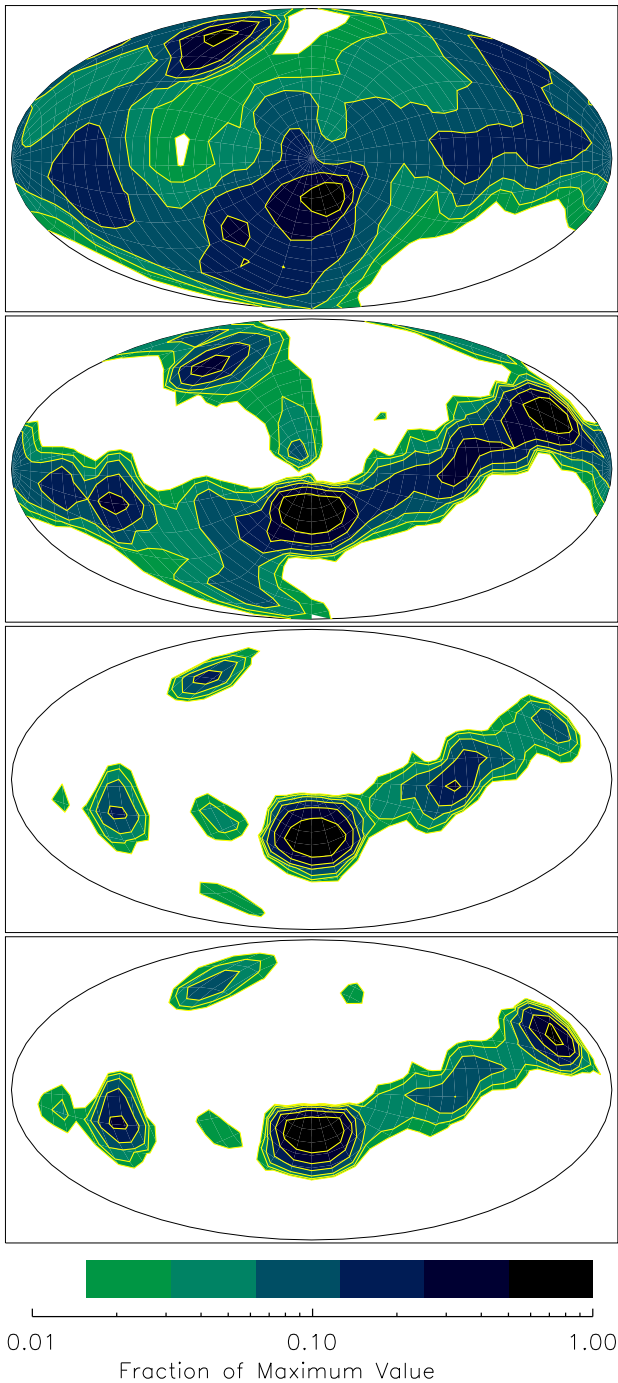
rich backbone. The lower panel of the Figure shows the backbone by itself, with gaps at the positions of some of the large galaxies. We expect galaxies to concentrate gas at their centers, and many in the simulation do. However, the central regions are usually too small to show up as baryon-rich on the adopted 6.5 kpc grid scale.

Figure 5 zooms in still further to show individual simulation particles. The upper panel shows just the gas particles concentrated into filaments. The lower panel shows the same field of view with just the dark matter particles. The dark matter, although broadly following the filaments, tends to assume quasi-spherical shapes.

#### 4 FILAMENTS RADIATE FROM CENTERS OF GALAXIES

. In section 3 we showed that the baryon-rich regions of the simulation form a system of filaments that connect the largest galaxies. In this section we explore the properties of the filaments in more detail by focussing on regions surrounding the 10 largest galaxies and the second largest galaxy in particular.

Figure 6 shows four images of a 55.4 kpc (proper) radius region centered on the second largest galaxy. The two upper images show the gas particles (left) and dark matter particles (right) that are bound to the galaxy as indicated by DENMAX. Each lower image shows the corresponding unbound particles. The three major spokes of bound gas in the upper left image are nearly coplanar.



**Figure 7.** Angular distribution of matter about the second largest galaxy, in Hammer-Aitoff projection. In descending order the maps show dark matter, gas, neutral hydrogen, and stars. Shown are contours of masses in the solid angles subtended by 192 HealPix pixels for a shell from 22.2 to 55.4 kpc. For each map there are six contour levels with a factor of two spacing. The highest contour for each map is one half the maximum of that map.

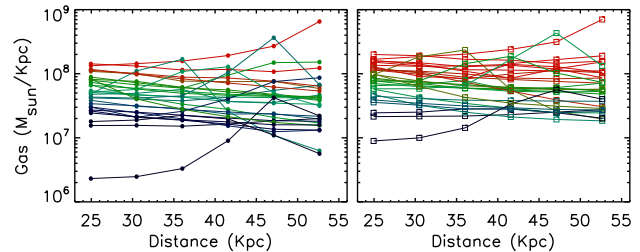


**Figure 8.** Linear density of gas along each of the 29 filaments around the 10 largest galaxies. Each curve represents one filament, and each point represents the gas contained in a segment of a coaxial cylinder around that filament of radius 8 kpc (left) or 16 kpc (right). See Figure 12 for a drawing of the geometry. The abscissa is distance from the galaxy center along the filament. The points are plotted at the centers of the segments.

To isolate individual filaments for quantitative study, we examine a shell extending from 22.2 kpc to 55.4 kpc around each of the 10 largest galaxies. The inner radius encompasses the bound region of the galaxy, while the outer radius is large enough to reveal the filamentary structure clearly, but not so large as to encroach on neighbouring large galaxies. On average, 10% of the solid angle of the shell contains 65% of the gas and 50% of the dark matter.

Figure 7 shows contour maps of a 192-pixel HealPix<sup>1</sup> tiling (Górski et al. 2005) of the shell around the galaxy in Figure 6. The dark matter (top panel) shows the smoothest distribution, while gas, neutral hydrogen, and stars (succeeding panels) are progressively more concentrated.

For objectivity we adopted a simple formal procedure for selecting the peak pixels that define the filaments. First we select those pixels that contain at least  $3.6 \times 10^8 M_{\odot}$  of gas. This minimum mass requirement is imposed so that a radial segmentation of a pixel into six equal parts is expected to contain at least  $6 \times 10^7 M_{\odot}$  of gas, which is more than one hundred times the fiducial mass of a gas particle in the simulation. Some smaller filaments, apparent to the eye, are thus omitted. Having made this selection, we refer to the contour maps to ensure that only one pixel, the maximum, is chosen from each contour peak. This procedure yields a total of 29 filaments around the 10 galaxies. Two of the 29 filaments overlap along their length, but the overlap is only about 30% of the length analyzed.

Figure 8 shows that the linear mass density of gas in the filaments generally varies along the filament by less than a factor of two or three. The range of values among the filaments is about an order of magnitude, with a few outliers. The Figure shows the mean density in cylinders of radius 8 and 16 kpc about a radial axis centered on the peak pixel.

Figure 9 shows further evidence that the properties of filaments do not vary greatly along their length. The Figure shows that the average cross-sectional profile of gas density and baryonic fraction of filaments is approximately independent of distance from the galaxy. Each of the three black curves with filled circles in each graph show the profile, averaged over all 29 filaments, of one of three equal segments spanning the distance from 22.2 to 55.4 kpc from the galaxy.

<sup>1</sup> We gratefully acknowledge the use of the HealPix software package obtained from <http://healpix.jpl.nasa.gov>.

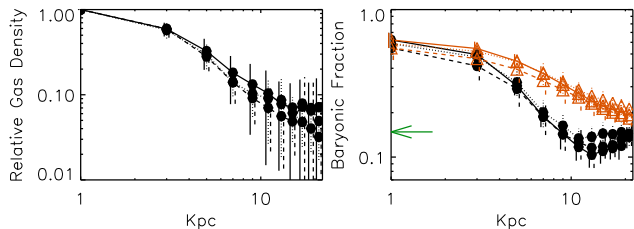


**Figure 9.** Average cross-sectional profiles of filaments at each of three distances from the galaxy. The left and right panels show respectively the gas density and baryonic fraction as a function of distance from the center of the filament. In the right panel the black curves with the black filled circles show the baryonic fraction in the individual radial bins, while the orange curves with the triangles show cumulative baryonic fractions for regions extending outward and including the bin. The green arrow in the right graph shows the cosmic mean baryon fraction. For these graphs, each filament from 22.2 to 55.4 kpc from the center of the galaxy was divided into 3 equal segments. Solid, dotted, and dashed lines show profiles for the inner, middle, and outer segments averaged over all 29 filaments. Gas densities and baryonic fractions were computed on cylindrical shells having a radial width of 2 kpc. In the left panel the data for each filament segment were normalized to the gas density in the lowest radial bin for that particular filament. Vertical lines show two sigma errors. Symbols are plotted at the centers of the radial distance bins.

The lower panel of Figure 9 shows that the average baryonic fraction (black curves with filled circles) exceeds twice the cosmic mean out to about 5 kpc, and remains above the cosmic mean out to about 9 kpc, beyond which it dips slightly below the mean. This is consistent with the idea that there has been a separation of baryons and dark matter, with baryons becoming more centrally concentrated in the filaments. The Figure also shows the cumulative baryonic fraction (orange curves with triangles) within the radius. The cumulative baryonic fraction remains elevated out to beyond 20 kpc. At least some of this enhanced baryon fraction can be attributed to sheets, described in the next section, at whose intersections the filaments are found.

## 5 FILAMENT ASSOCIATED SHEETS

Radiating from the filaments are thin sheets of gas. Figure 10 shows three sheets extending from a single filament of the galaxy shown in Figure 6. The images on the left show gas particles, and those on the right dark matter particles. The top panel shows a projection on to a plane perpendicular to the filament, with the filament in the center. The top left image shows the three sheets edge on. The lower left image shows this complex from another angle so that the three sheets are fully visible. The filament lies at the intersection of the three sheets. Outlines of a surrounding box are shown to enhance the three-dimensional effect. The filament is perpendicular to the front face of this box. The image on the lower right shows the same view as on the left but with dark matter particles only. There is some tendency for the dark matter to concentrate in the vicinity of the sheets, but it tends to form quasi-spherical haloes rather than the thin, extended sheets formed by the gas.

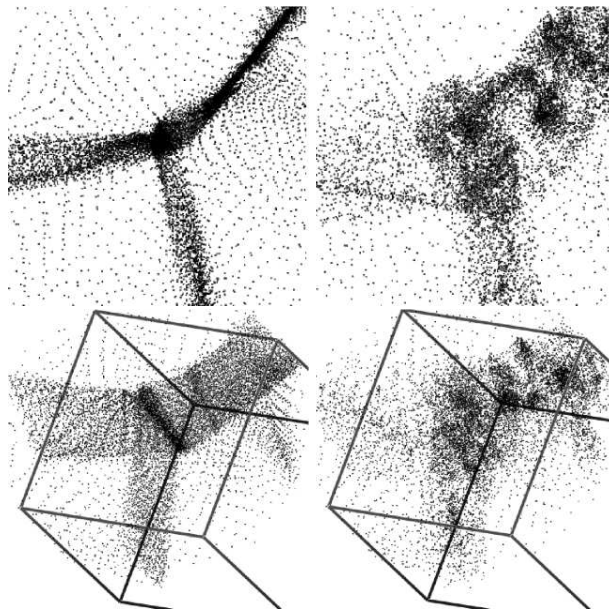


**Figure 10.** Sheets of gas radiating from a filament. Shown is the distribution of gas and dark matter around the axis of a filament from the galaxy shown in Figure 6. Upper panel shows gas particles (left) and dark matter particles (right) in a projection on to a plane perpendicular to the filament. The axis of the filament is at the center going into the page. In the lower panel these structures are shown at a different angle to show the three sheets formed by the gas particles (left) and the more irregular distribution of the dark matter particles (right). The dimension of each square image, and of the box, is 110.8 kpc proper.

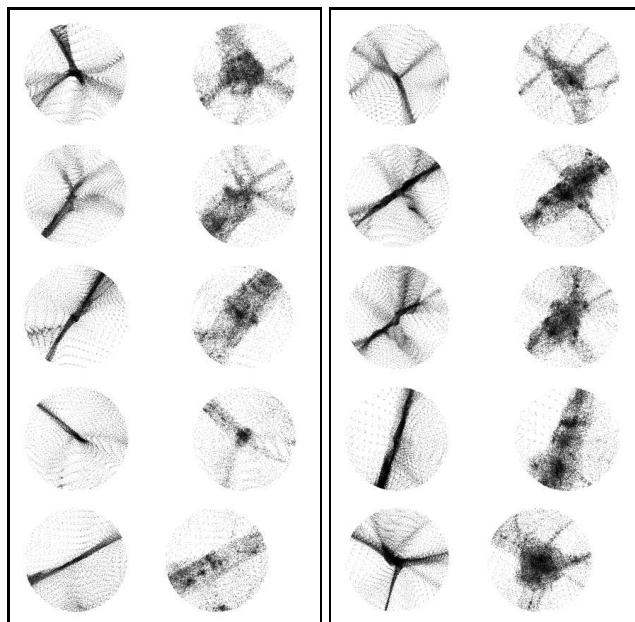


**Figure 11.** Sheets of gas radiating from the other filaments around the three largest galaxies. Each horizontal pair of images represents the same filament with the gas particles on the left and the dark matter particles on the right. Each filament is viewed as a projection on a plane perpendicular to the filament with the filament in the center going into the page. Each image is 110.8 kpc on a side. Only the portion along the filament from 22.2 to 55.4 kpc from the center of the galaxy is shown.

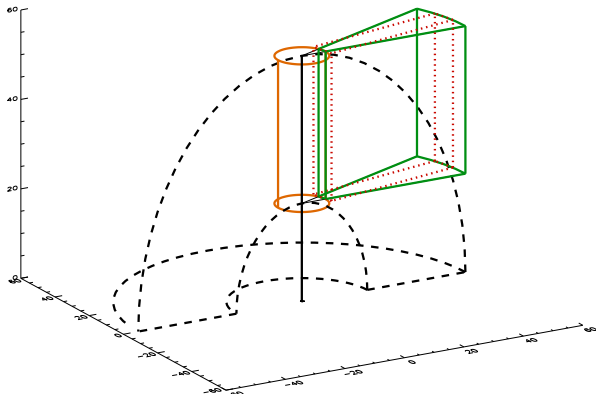


**Figure 12.** Cutaway of analyzed regions surrounding a galaxy. The solid vertical line represents a filament extending 55.4 kpc from the center of a galaxy at its lower end. The dashed black lines show the shell about the galaxy that contributes to the HealPix contour map. Linear density along the filament is computed for the 8 kpc orange cylinder. The green wedge portrays one of the 16 radial sectors used to select the sheets. The red dotted box depicts a slab centered on a selected sheet.

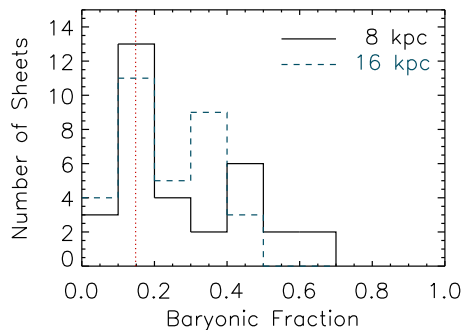


**Figure 13.** Histograms of the baryonic fractions of the 32 sheets around the 29 filaments. These fractions are calculated on slabs 8 and 16 kpc in thickness centered on the sheet (see Figure 12). The region considered for each sheet extended from 8 to 55 kpc from the filament in a perpendicular direction and between 22.2 and 55.4 kpc from the galaxy along the filament. The vertical dotted red line marks the cosmic mean baryon fraction.

Figure 11, a montage of images of the remaining 10 filaments from the three largest galaxies (omitting the one shown in Figure 10), gives an idea of the variation seen. Each image is a view centered on a single filament running perpendicular to the page. The images are arranged in horizontal pairs with the gas particles shown on the left and the dark particles on the right. The spokes of gas radiating from the filament are the sheets seen edge on. Viewed face on, the sheets resemble those in the image in the lower left section of Figure 10. Although dark matter clusters near the sheets, it is more diffusely distributed than the gas.

To quantify the gas density and baryonic fraction of the sheets, we averaged over rectangular slabs whose geometry and selection is diagrammed in Figure 12. To select sheets, we take a cylinder of radius 55.4 kpc coaxial with each filament, and divide it into 16 equal angular sectors. We exclude from the volume analyzed an inner cylinder of radius 8 kpc to eliminate the central region of the filament itself.

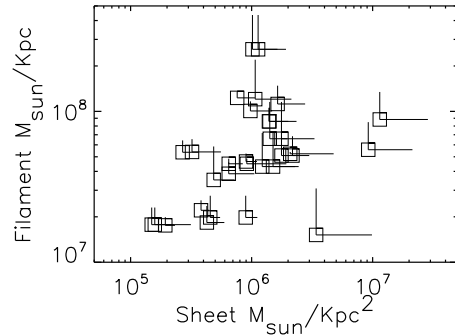


**Figure 14.** Surface density of gas in sheets compared to the linear density of the parent filament. Horizontal and vertical lines show the standard deviations of the densities obtained from averaging nine equal rectangles of the sheet. For clarity in a log-log plot only the error bars on the positive sides of each data point are drawn. Each rectangle measures 11.1 kpc in the direction of the filament and 15.8 kpc along the sheet in a direction perpendicular to the filament. The innermost boundary of the region analyzed is a cylinder of radius 8 kpc coaxial with the filament. This limit is used to exclude material from the filament itself.

We select as a sheet those sectors that contain at least 20% of the gas mass in the cylindrical shell. Having identified a sheet in this fashion, we measure the gas density and baryon fraction in a rectangular slab extending from 8 to 55 kpc away from the filament, and either 8 or 16 kpc in thickness.

This selection process produced 32 sheets from the 29 filaments around the 10 largest galaxies. Figure 13 shows the baryonic fraction of each sheet, measured in slabs of thickness 8 or 16 kpc centered on the sheets. The Figure shows that there is a tendency for the sheets to be enriched in baryons.

Figure 14 compares the surface density of gas of each of the 32 sheets with the linear density of gas in the associated filament. The surface densities of gas vary over a range two orders of magnitudes and have a positive correlation with the filament densities that is marginally significant at the  $2\sigma$  level<sup>2</sup>.

## 6 DISCUSSION AND CONCLUSIONS

Using a high resolution cosmological simulation of reionization, we have found evidence for a significant population of baryon-rich filaments at a redshift of 5.1. The filaments are associated with the largest galaxies, and can be found radiating away from their centers. The baryon-rich filaments are at the intersections of sheets, which also tend to be enriched in baryons. The dark matter is distributed more irregularly, tending to form quasi-spherical bodies.

The present work helps to fill a somewhat neglected gap between the linear regime of gravitational collapse and the highly nonlinear regime of galactic interiors. Our investigation has highlighted the contrasting distribution of baryons

<sup>2</sup> Spearman's rho for rank correlation is 0.53, which for a two-tailed distribution is significant at the 95% level. To compute this, sheets attached to the same filament were averaged, resulting in 15 pairs for rank order analysis.

and dark matter on  $\sim 6$  kpc scales where hydrodynamic processes are important, but intergalactic structure is still readily delineated. The simulation investigated in this paper was originally carried out in order to explore reionization, and therefore includes detailed baryonic physics, including 3-dimensional radiative transfer of ionizing radiation self-consistently generated by star formation, that is often neglected in other kinds of cosmological simulation. The results point to a need for careful treatment of baryonic processes in modeling moderately nonlinear scales.

At large, linear scales, baryons and dark matter are expected to follow the same distribution. In the opposite limit of small, highly non-linear scales, the baryonic fraction within the virial radius of a collapsed halo is close to the mean (Crain et al. 2007). It may therefore seem surprising that at intermediate, mildly non-linear scales, the difference between the distribution of baryons and dark matter can be as prominent as found in this paper. Linear theory predicts that initially the difference in the clustering of baryons and dark matter is described by a filtering scale (Gnedin & Hui 1998), below which pressure forces tend to smooth the baryons compared to the dark matter. The present simulation indicates that, at least in regions where the separation of baryons and dark matter is most marked, the separation is more complex, and anisotropic. Baryons tend to concentrate toward the centers of filaments and sheets, in directions perpendicular to the filament or sheet, but are more smoothly distributed than dark matter in directions along the filament or sheet. The central concentration of baryons compared to dark matter is consistent with simple models of one-dimensional collapse into filaments and sheets (Shandarin & Zel'dovich 1989; Anninos et al. 1995) although this consistency is perhaps surprising given that evolution is much more complicated in three dimensions than in one. Another unexpected finding is that the baryon-rich filaments and sheets remain coherent over scales much larger than the filtering scale of 4 kpc proper (24 kpc comoving) predicted at this redshift by Gnedin et al. (2003).

Undoubtedly much of the difference between baryons and dark matter in the simulation reported in this paper can be attributed to the fact that baryons are collisional whereas dark matter is collisionless: parcels of collapsing gas cannot pass through each other, whereas dark matter can. Probably another important effect is that the energy of collapse of the baryons into filaments and sheets is channelled into gas pressure, mediated at least in part by co-axial shocks, as suggested by Cen et al. (1994), Miralda-Escudé et al. (1996), and Zhang et al. (1998), which can smooth the baryons in directions along the filaments and sheets.

The baryon-rich filaments may have important implications for our understanding of structure formation in the universe. First, charting the course of reionization depends heavily upon uncertain assumptions about the escape fraction of ionizing radiation from galaxies. The highly aspherical distribution of the surrounding gas should be taken into account in mapping the journey of such a photon from its origin near the center of the galactic halo. In this regard it is interesting that the filaments appear to extend essentially unaltered into nearly the center of the galaxy.

Second, the filaments are likely to be important in the process of gas accretion on to galaxies. As discussed

by Kereš et al. (2005, and references therein), two general modes of accretion are distinguished, a hot mode and a cold mode. In the hot mode, which dominates the growth of the largest galaxies, gas, shock heated to the virial temperature of the dark matter halo, accretes in a spherically symmetric fashion. In the cold mode, which dominates for smaller galaxies, such as those seen in our simulation, gas accretes in a directional manner, often along filaments (Kawata & Rauch 2007). The filaments we see are obvious candidates for cold accretion conduits. Since the ability of a galaxy to accrete gas is important for sustained star formation, the evolution of these structures may in turn help us to understand the star formation history of the universe.

Third, the planar distribution of Milky Way satellite galaxies may have resulted from an early sheet (Libeskind et al. 2005), possibly of the kind described in this paper.

The baryon-rich structures discussed in this paper may be potentially observable in the Lyman alpha forest (for reviews see Rauch 1998; Meiksin 2007), although a precise assessment of their observational impact will require further work that goes beyond the scope of this paper. Descendants of these structures may play a role in producing the warm-hot intergalactic medium (WHIM), thought to be a major reservoir of baryons in the low redshift universe (Davé et al. 2001).

## ACKNOWLEDGMENTS

This work was supported in part by the DOE and NASA grant NAG 5-10842 at Fermilab, by NSF grants AST-0134373 and AST-0507596, and by the National Computational Science Alliance grant AST-020018N, and utilized IBM P690 arrays at the National Center for Supercomputing Applications (NCSA) and the San Diego Supercomputer Center (SDSC).

## REFERENCES

- Anninos W. Y., Norman M. L., Anninos P., 1995, *ApJ*, 450, 1
- Barkana R., Loeb A., 2007, *Reports of Progress in Physics*, 70, 627
- Bertschinger E., Gelb J. M., 1991, *Computers in Physics*, 5, 164
- Bond J. R., Kofman L., Pogosyan D., 1996, *Nature*, 380, 603
- Cen R., Miralda-Escudé J., Ostriker J. P., Rauch M., 1994, *ApJL*, 437, L9
- Crain R. A., Eke V. R., Frenk C. S., Jenkins A., McCarthy I. G., Navarro J. F., Pearce F. R., 2007, *MNRAS*, 377, 41
- Davé R., Cen R., Ostriker J. P., Bryan G. L., Hernquist L., Katz N., Weinberg D. H., Norman M. L., O'Shea B., 2001, *ApJ*, 552, 473
- Gnedin N. Y., 1995, *ApJS*, 97, 231
- Gnedin N. Y., Abel T., 2001, *New Astronomy*, 6, 437
- Gnedin N. Y., Baker E. J., Bethell T. J., Drosback M. M., Harford A. G., Hicks A. K., Jensen A. G., Keeney B. A., Kelso C. M., Neyrinck M. C., Pollack S. E., van Vliet T. P., 2003, *ApJ*, 583, 525

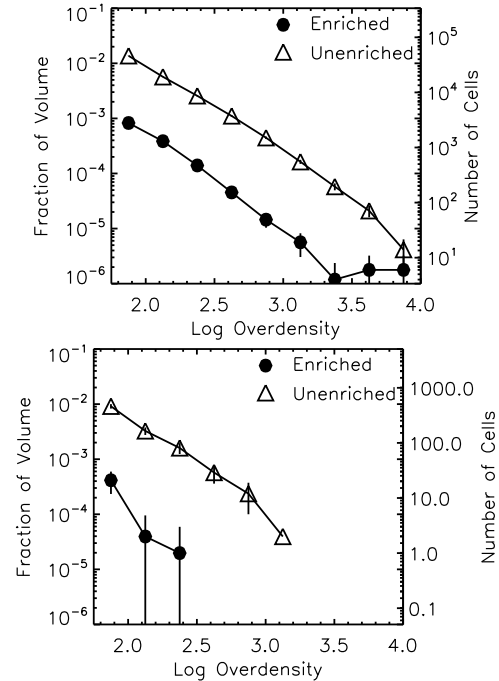


Gnedin N. Y., Bertschinger E., 1996, ApJ, 470, 115  
 Gnedin N. Y., Fan X., 2006, ApJ, 648, 1  
 Gnedin N. Y., Hui L., 1998, MNRAS, 296, 44  
 Górski K. M., Hivon E., Banday A. J., Wandelt B. D., Hansen F. K., Reinecke M., Bartelmann M., 2005, ApJ, 622, 759  
 Harford A. G., Gnedin N. Y., 2003, ApJ, 597, 74  
 Harford A. G., Gnedin N. Y., 2007, ApJ, 664, 599  
 Hernquist L., Katz N., Weinberg D. H., Miralda-Escudé J., 1996, ApJL, 457, L51  
 Jing Y. P., Suto Y., 2002, ApJ, 574, 538  
 Kawata D., Rauch M., 2007, ApJ, 663, 38  
 Kereš D., Katz N., Weinberg D. H., Davé R., 2005, MNRAS, 363, 2  
 Kohler K., Gnedin N. Y., 2007, ApJ, 655, 685  
 Libeskind N. I., Frenk C. S., Cole S., Helly J. C., Jenkins A., Navarro J. F., Power C., 2005, MNRAS, 363, 146  
 Lin C. C., Mestel L., Shu F. H., 1965, ApJ, 142, 1431  
 Meiksin A. A., 2007, ArXiv e-prints, 711  
 Miralda-Escudé J., Cen R., Ostriker J. P., Rauch M., 1996, ApJ, 471, 582  
 Rauch M., 1998, ARA&A, 36, 267  
 Schmalzing J., Buchert T., Melott A. L., Sahni V., Sathyaprakash B. S., Shandarin S. F., 1999, ApJ, 526, 568  
 Shandarin S. F., Doroshkevich A. G., Zel'dovich I. B., 1983, Soviet Physics Uspekhi, 139, 83  
 Shandarin S. F., Melott A. L., McDavitt K., Pauls J. L., Tinker J., 1995, Physical Review Letters, 75, 7  
 Shandarin S. F., Zel'dovich Y. B., 1989, Reviews of Modern Physics, 61, 185  
 Shen J., Abel T., Mo H. J., Sheth R. K., 2006, ApJ, 645, 783  
 Sheth J. V., Sahni V., Shandarin S. F., Sathyaprakash B. S., 2003, MNRAS, 343, 22  
 Spergel D. N., Verde L., Peiris H., et al. 2003, ApJS, 148, 175  
 Valinia A., Shapiro P. R., Martel H., Vishniac E. T., 1997, ApJ, 479, 46  
 Zel'dovich Y. B., 1970, A&A, 5, 84  
 Zhang Y., Meiksin A., Anninos P., Norman M. L., 1998, ApJ, 495, 63

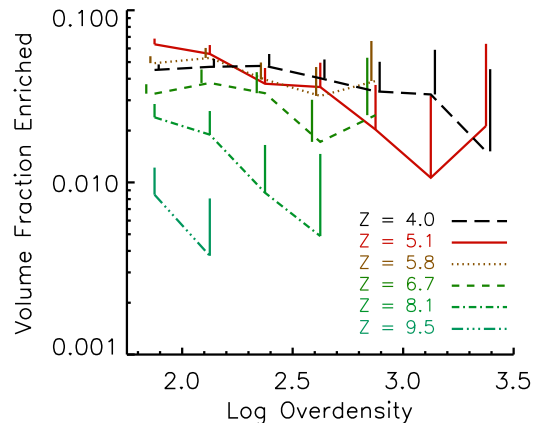
**APPENDIX A: VARYING CELL SIZE AND REDSHIFT**

Figure A1 shows the volume fractions enriched in baryons for grid cell sizes of 4.1 and 16.3 kpc proper (25 and 100 kpc comoving) at a redshift of 5.1. These graphs are to be compared to Figure 3, which shows the results for the 6.52 kpc (40 kpc comoving) cell size used predominantly in the paper. The results for a grid cell size of 4.1 kpc are consistent with those at 6.52 kpc. We preferred the larger cell size because estimates of the baryon fraction in each cell are more accurate, especially at lower overdensities. Increasing the cell size to 16.3 kpc leads to a considerable loss of baryon-rich cells. This is consistent with the  $\sim 5$  kpc radius of filaments illustrated in Figure 9.

Figure A2 compares the baryon-rich fraction over a range of redshifts (the data for  $z = 4$  was obtained from a lower resolution simulation). Baryonic enrichment appears



**Figure A1.** Effect on baryonic fraction of varying the grid cell size. Same as Figure 3, but for cell sizes of 4.1 kpc proper (25 kpc comoving) in the upper graph, and 16.3 kpc proper (100 kpc comoving) in the lower graph.



**Figure A2.** Volume fraction of baryon-enriched regions as a function of overdensity, at several redshifts. As elsewhere in this paper, the threshold for baryon-enrichment is taken to be twice the cosmic mean. The cell size for all redshifts is 40 kpc comoving. Vertical lines show two sigma errors (only the upper error bars are shown).

generally to increase with time. Computational limitations prevent us from evolving the simulation to lower redshifts.